

Diagnostic applications of Raman spectroscopy

Qiang Tu, MS^a, Chang Chang, PhD^{a,b,*}

^a*School of Biomedical Engineering, Science and Health Systems, Drexel University, Philadelphia, Pennsylvania, USA*

^b*Department of Radiation Oncology, University of Pennsylvania, Philadelphia, Pennsylvania, USA*

Received 31 March 2011; accepted 24 September 2011

Abstract

Raman spectroscopy has been widely used in various fields of science. It has been successfully utilized to qualitatively and quantitatively determine the molecular compositions of solid, liquid, and gaseous samples. This review focuses on the diagnostic applications of Raman spectroscopy in the past 5 years, with specific emphasis on transplant allograft rejection and cancer detections. First we introduce the principle of Raman spectroscopy and associated surface enhancement techniques. Various recent biomedical and clinical applications of Raman spectroscopy are then reviewed in detail. Finally, we present the experimental and analytical techniques required to implement Raman spectroscopy in a laboratory.

From the Clinical Editor: This review focuses on evolving diagnostic applications of Raman spectroscopy with special emphasis on transplant allograft rejection and cancer detection.

© 2012 Elsevier Inc. All rights reserved.

Key words: Raman spectroscopy; SERS; Cancer diagnosis; Transplant rejection

Early and accurate detection of diseases permits effective intervention. It also facilitates efficacious therapy and monitoring of therapeutic progression, and can reduce mortality and morbidity. New detection technologies that are reliable and of high specificity and sensitivity are therefore always being sought for disease diagnosis and severity grading. Raman spectroscopy, with its molecular specificity and various signal enhancement techniques for increased sensitivity, has been extensively utilized in biomedical and clinical applications.^{1,2} Both in vivo and in situ measurements have been demonstrated with minimum or no sample preparation. Recently Raman spectroscopy has been utilized to track nanomaterials moving through the circulation,^{1,3,4} and to detect inhaled nanoparticles in the respiratory tract.⁵ Quantitative Raman spectroscopy has also been used for the severity grading of various cancers.^{6–8} In addition, with the help of surface enhancement techniques, applications of Raman spectroscopy have seen a steady increase in various areas of nanomedicine such as the detection of cancer cells tagged with nanotubes or other nanostructures.^{9–12} As Raman spectroscopy continues to find wider applications, this review aims to facilitate the use of Raman spectroscopy as an analytical tool in a typical biomedical laboratory by introducing its

principles, current applications, and necessary quantitative and experimental techniques. Table 1 summarizes the applications of Raman spectroscopy reviewed in this article, including the types of analysis, experimental apparatus, and analysis methods.

Principles of Raman spectroscopy

Raman spectroscopy typically uses a nonionizing laser as the excitation source. The incident photons can be absorbed, scattered, and/or pass through the material without interaction. If the energy of the incident photon matches the energy gap between the ground state and an excited state of a molecule, the photon will most likely be absorbed and the molecule is promoted to the excited state. Fluorescence occurs when the excited molecule subsequently relaxes to the ground state by emission. Scattering takes place, on the other hand, as the incident photon distorts the electron clouds. Two types of scattering typically exist in the visible-light and near-infrared spectral range: Rayleigh and Raman scattering. The more intense form, Rayleigh scattering, happens when only the electron clouds are distorted. This is considered an elastic process, as no appreciable energy exchange occurs. However, if the vibrational state of the molecule is altered, energy transfer occurs, either from the photon to the molecule or vice versa. The process becomes inelastic and is named Raman scattering. This is in general a weak process involving approximately one in every 10^6 – 10^8 scattered photons.^{1,13,14}

Sources of support: Wallace H. Coulter Foundation Translational Research Grant.

*Corresponding author: Department of Radiation Oncology, University of Pennsylvania, Philadelphia, PA 19104, USA.

E-mail address: chang.chang@uphs.upenn.edu (C. Chang).

1549-9634/\$ – see front matter © 2012 Elsevier Inc. All rights reserved.
doi:10.1016/j.nano.2011.09.013

Table 1
Diagnostic applications of Raman spectroscopy

Raman application		Experimental setup			Analysis method	Reference
		Wavelength (nm)	Power (mW)	Exposure time (sec)		
Cancer detection	Breast cancer	830	100–150	10–30	Nonnegative least square (NNLS)	8
		830	82–125	1	Probe NNLS	31
		786	N/A	4	Raman shifts	7
		830	65	10	PCA-LDA	34
		514.5	8	N/A	Hierarchical cluster	42
	Cervical cancer	785	80	5–15	Probe Logistic regression	45
		785	80	5	Probe Maximum representation and discrimination feature (MRDF)	47
	Colorectal cancer				Sparse multinomial logistic regression (SMLR)	
		785	15	60	Probe PCA-LDA	49
		785	10	60	Raman shifts	43
		785	100	30	PCA	50
		785	300	5	Probe PCA-Support vector machines (SVMs)	51
		785	70	N/A	PCA	35
					Hierarchical cluster	
					Multiple least squares (MLS)	
		782.5	11.5	60	LTRS PCA-Logistic regression	52
		782.5	11.5	60	LTRS PCA-Artificial neural network (ANN)	53
		785	100	10	PCA	54
Allograft rejection	Cardiac rejection	785	100	10	PCA	54
	Renal rejection	785/514.5	8–12	10	PCA-Discriminant function analysis (DFA)	56
SERS for biomarker		785	100	20	NNLS	65
		785	25	10	Raman shifts	66
		633	N/A	N/A	Raman shifts	9
SERS for in vivo		785	50	120	Partial least squares	75
		785	20	2	Raman shifts	10
SWNTs		N/A	100	2	Raman imaging using G-band	88
		785	100	3/10	Raman imaging using G-band	91
		785	80	0.5	Raman imaging using G-band	94
SERS imaging		785	60	N/A	Raman imaging using SERS peaks	100
		633	N/A	N/A	Raman imaging using SERS peaks	101
Core-shell nanoparticle		633	0.5/4	30/60	Raman shifts	105
		633	2	50	Raman shifts	109
		633	0.3	10	Raman shifts	110

Depending on the direction of energy transfer between the molecule and the photon, Raman scattering can be further categorized into two subtypes: Stokes and anti-Stokes. Stokes scattering takes place when the molecule absorbs energy from the incident photon and elevates itself from a lower energy state to an excited vibrational state. On the other hand, because of thermal perturbation or prior external excitation, the molecule may already be in an excited vibrational state before interacting with the incident photon. In this case anti-Stokes scattering may result, such that the molecule releases energy upon interacting with the incident photon and subsequently returns to a lower energy state. The scattered photons in an anti-Stokes process therefore are of higher energy than the incident photons. Because at room temperature most molecules are in the ground state, Stokes scattering typically dominates. Stokes scattering is therefore commonly recorded for Raman spectroscopy unless special experimental conditions are arranged. Raman band shifts (i.e., the energy difference between the incident and scattered photons) are typically described in wavenumber. The most commonly used unit to

denote wavenumber is cm^{-1} , and it is equivalent to joule by a conversion factor (hc), where h is the Planck constant and c is the speed of light. Figure 1 illustrates the Rayleigh, Stokes, and anti-Stokes scattering processes.

A typical laboratory Raman spectroscopy system is shown in Figure 2. The incident laser irradiates the sample via an optical microscope, and the Raman scattered photons are collected into a spectrometer following appropriate filtering. Lasers at various visible-light and near-infrared wavelengths can be used as the excitation source. For example, a HeNe laser has a wavelength of 633 nm, and a Ti:sapphire laser is tunable from 650 nm to 1100 nm. When examining biological samples, longer wavelength excitations typically produce less fluorescence background and are therefore preferred.

Surface-enhanced Raman spectroscopy (SERS) increases the Raman signal level by exploiting the interaction between the molecule and a nanoscale metal surface. Raman signals thus emitted are strongly enhanced by a factor of 10^3 – 10^{14} , depending on the definition of the enhancement factor.^{15,16} For substrate-based surface-enhanced Raman spectroscopy (SERS)

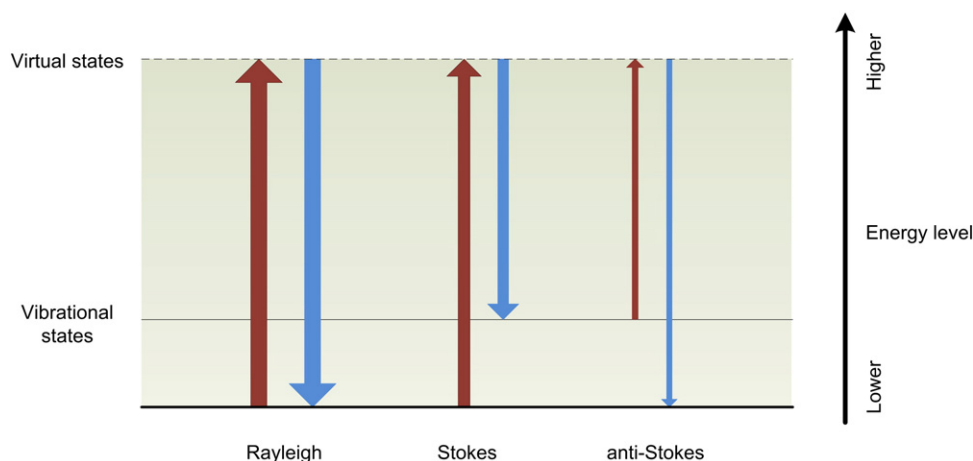


Figure 1. Energy diagram for Rayleigh and Raman scattering processes. Rayleigh scattering is the most intense scattering process, and Stokes scattering predominates over anti-Stokes scattering at room temperature. Thickness of the arrows indicates the relative intensity of the three processes (not to scale).

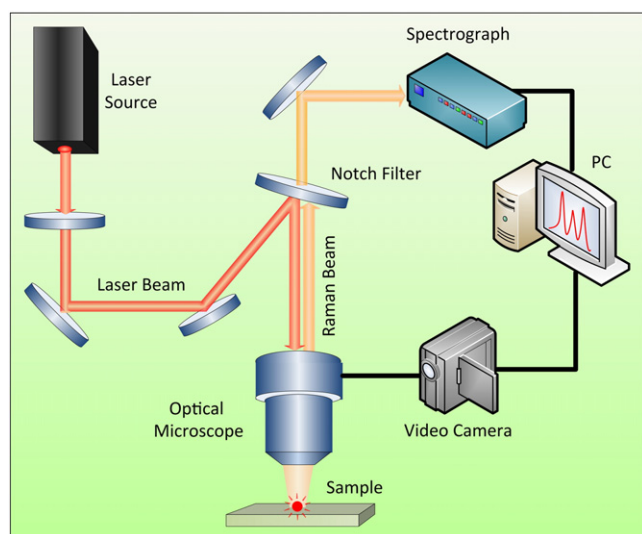


Figure 2. A typical laboratory Raman spectroscopy system. PC, personal computer.

experiments, the most widely used definition for average SERS enhancement factor is

$$EF = \frac{I_{\text{SERS}} / N_{\text{Surf}}}{I_{\text{RS}} / N_{\text{Vol}}},$$

where I_{SERS} and I_{RS} are the SERS and regular Raman intensity, respectively. N_{Vol} is the average number of molecules in the scattering volume for regular Raman, and N_{Surf} is the average number of adsorbed molecules in the scattering volume for SERS. For SERS in colloidal solutions, the analytical enhancement factor or apparent enhancement factors (AEFs) are calculated by

$$AEF = \frac{I_{\text{SERS}} / C_{\text{SERS}}}{I_{\text{RS}} / C_{\text{RS}}}$$

where I_{SERS} and I_{RS} are SERS and regular Raman intensities of normalized Raman spectra at the selected band, respectively. C_{SERS} and C_{RS} are concentrations of the target molecule in colloidal and

aqueous solutions, respectively. SERS is capable of detecting molecules in extremely low concentrations, making it an attractive technique for biomedical applications.

Although the exact theoretical foundation of SERS is still illusive, it is generally agreed that SERS consists of two major underlying physical mechanisms: the electromagnetic field effect and the chemical charge transfer effect.^{17,18} The electromagnetic effect is a result of the excitation of surface plasmon by the incident laser, whereas the charge transfer effect is caused by the electron exchange between the molecule and the metal colloid.¹⁹ Surface plasmon is the resonant oscillation of conduction electrons on a metal surface induced by an electromagnetic field. It is well known that the exposure of surface plasmon to laser irradiation increases the lattice temperature,^{20,21} and this surface plasmon-induced heat generation has been identified as the potential cause of SERS signal reduction seen in prolonged irradiation of nanoparticles.²² Note that because SERS results from the interaction between the molecule under test and the nanoscale metal surface, the band shifts, relative peak intensity, and peak bandwidths in the SERS spectra are different from those in the Raman spectra of the same molecule.

Cancer detection

Cancer is the second most common cause of death in the United States.²³ Efficacious cancer treatments rely on early detection and accurate diagnosis. Various Raman spectroscopic studies on cancers have been reported,^{24–29} and here we review its use on the three most commonly seen carcinomas—breast, colorectal, and cervical cancers.

Breast cancer

Breast cancer had the highest rate of occurrence in the United States among the female population in 2010.²³ Numerous studies have investigated the application of Raman spectroscopy on the detection of normal, precancerous and cancerous breast tissues.^{8,30–33} For instance, Haka and colleagues have demonstrated the ability of Raman spectroscopy to distinguish between normal, benign, and malignant lesions of breast ex vivo, with a sensitivity of 94% and a specificity of 96%.⁸ Tissues in four

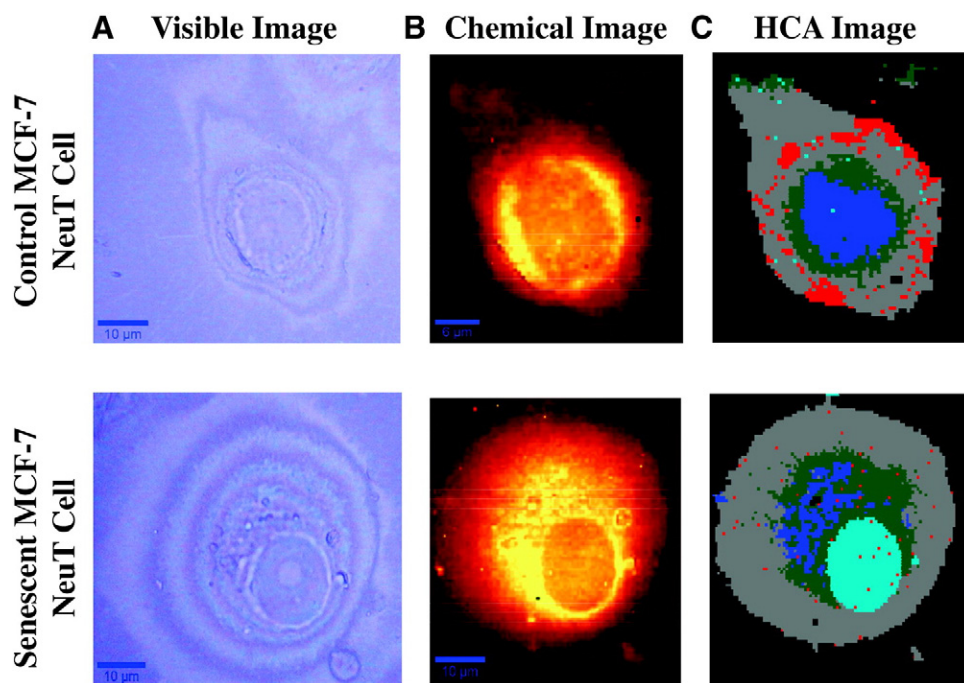


Figure 3. Visual (A) and Raman imaging (B, C) of single control and senescent MCF-7/NeuT cells. Raman images (B) were composed specifically from CH-stretching and were analyzed using (C) unsupervised hierarchical cluster analysis (HCA). Reprinted with permission.⁴² Copyright 2010 American Chemical Society.

pathological conditions were examined and classified, including normal, fibrocystic change, fibroadenoma, and infiltrating carcinoma. Raman spectra of breast tissues were fitted to those of individual breast tissue components including fat, collagen, cell nucleus, epithelial cell cytoplasm, calcium oxalate, calcium hydroxyapatite, cholesterol-like lipid deposits, and β -carotene. This approach is based on the assumption that the Raman spectrum of a mixture is a linear combination of the spectra of its components. Variations in the fitting coefficients reflect the chemical and morphological changes of the breast tissue due to carcinogenesis. Fitting coefficients of fat and collagen have been identified as the key parameters used for diagnostic differentiation. Normal breast tissues are composed of fat predominantly, and all abnormal breast tissues show an increased percentage of collagen, due to the formation of fibrosis. Fibroadenoma can then be further separated from infiltrating carcinoma by its lower fat content, because fibroadenoma grows by pushing the fat aside whereas infiltrating carcinoma infiltrates between fat cells and retains the fat in situ. These results are consistent with known breast pathology and therefore validate the use of Raman spectroscopy for breast cancer detection *ex vivo*. The clinical potential of Raman spectroscopy was also demonstrated by the same authors with the use of an optical fiber probe for *in vivo* Raman studies.³¹ The spectral data were analyzed in real time, and the diagnosis results were displayed intraoperatively.

Rehman and co-workers quantitatively examined the Raman spectral differences between different grades of invasive ductal carcinoma and ductal carcinoma *in situ*.⁷ For both pathologies, the spectral intensity of selected Raman peaks increased with advancing grades, indicating Raman spectroscopy's potential for quantitative carcinoma grading.

Instead of examining breast tissues directly, Pichardo-Molina's group studied serum samples from breast cancer patients and demonstrated the use of Raman spectroscopy for minimally invasive diagnostics.³⁴ Seven Raman band ratios were used for classification, and spectral differences were observed between serum samples of breast cancer patients and normal healthy subjects. Using principal component analysis (PCA) and linear discriminant analysis (LDA), the sensitivity and specificity were reported to be 97% and 78%, respectively. However, the underlying molecular mechanism of these differences were not reported.

Raman spectroscopic imaging technique has gained popularity recently in cancer research.^{35–39} Comparing with other standard imaging methods such as immunofluorescence and immunohistochemistry, Raman spectroscopic imaging is capable of visualizing the samples without extrinsic labeling, thus minimizing sample perturbation. In addition, the much-needed chemical and structural information about the sample are provided by Raman spectral analysis.^{40,41} Mariani and co-workers have applied Raman imaging to the detection of nuclear membrane lipid fluctuations in senescent epithelial breast cancer cells.⁴² In this study, Raman images were composed based on the Raman peak intensity of CH-stretching (Figure 3, B). Subcellular localities such as the nucleus were accurately imaged, and differences in lipid and glycoprotein components were detected.

Cervical cancer

Cervical cancer is the second most common malignancy in women worldwide, with more than half a million cases diagnosed and approximately 288,000 cervical cancer-related deaths each year.⁴³ Currently Papanicolaou (Pap) smear is the

most commonly used screening method for cervical cancer, with a detection specificity of 96.8%, but a sensitivity of only 55.4%.⁴⁴ Raman research in this area has focused on achieving comparable or better specificity and sensitivity numbers than the Pap smear.

Algorithms were designed to discriminate between normal and diseased cervical tissues. Using a logistic regression algorithm, Robichaux-Viehoever et al were able to distinguish high-grade dysplasia from benign tissues with a sensitivity of 89% and a specificity of 81%.⁴⁵ The spectra were collected in vivo using a fiber-optic probe.⁴⁶ Employing nonlinear algorithms, Kanter and colleagues achieved a sensitivity of 98% and a specificity of 96%.⁴⁷ They have also reported that by incorporating into their algorithm the patient's hormonal status, particularly the menstrual cycle and the menopausal state, the classification accuracy can be further improved.⁴⁸

New experimental techniques have also been used to improve detection accuracy in cervical cancer. Whereas most Raman studies are performed in the “fingerprint” spectral region with wavenumbers below 1500 cm^{-1} (ref. 13), Mo and colleagues have investigated the high-wavenumber region (2800–3700 cm^{-1}) for cervical cancer diagnosis, and achieved a diagnostic specificity and sensitivity of 97.8% and 93.5%, respectively.⁴⁹ Kamemoto's group compared the use of both fingerprint (775–975 cm^{-1}) and high-wavenumber regions (2800–3100 cm^{-1}) for in vitro cervical cancer detection, and found that Raman bands in the low-wavenumber region (Figure 4, B) provide more information on specific molecular and chemical changes in the tissue, whereas Raman spectra in the high-wavenumber region (Figure 4, C) have higher detection sensitivity due to stronger Raman signals and significantly less fluorescence background from the optical fibers.^{43,49}

Molecular etiology of the observed Raman spectral differences between normal and diseased cervical tissues was also studied.^{43,50} Comparison between normal and malignant cervical tissues showed that Raman spectra from normal cervical tissues feature characteristics of structural proteins such as collagen. For malignant cervical tissues, sharper amide I, minor red shift in ΔCH_2 , and sharper amide III indicated the presence of DNA, lipids, and noncollagen proteins.

Colorectal cancer

Colorectal cancer is the third most common malignancy in the United States.²³ An estimated 142,570 new cases and 51,370 related deaths are expected for 2010. Current standard of practice utilizes a white-light endoscope to screen and excise biopsy specimens in suspected sites. Difficulty exists in that early neoplasia and subtle lesions might evade the endoscopic survey, and biopsies are impractical for patients with multiple suspicious lesions.⁵¹ Optical biopsy using Raman spectroscopy is therefore an attractive alternative. Several groups have thus investigated and developed effective detection and classification algorithms. Widjaja and colleagues, for instance, combined PCA and support vector machines to classify different types of pathological colonic tissues, including normal, polyps, and cancers. Sensitivity and specificity greater than 98% have been reported.⁵¹ Beljebbar et al investigated the spatial distribution of molecular changes on the adenocarcinoma ex vivo.³⁵ Pseudo-color maps of

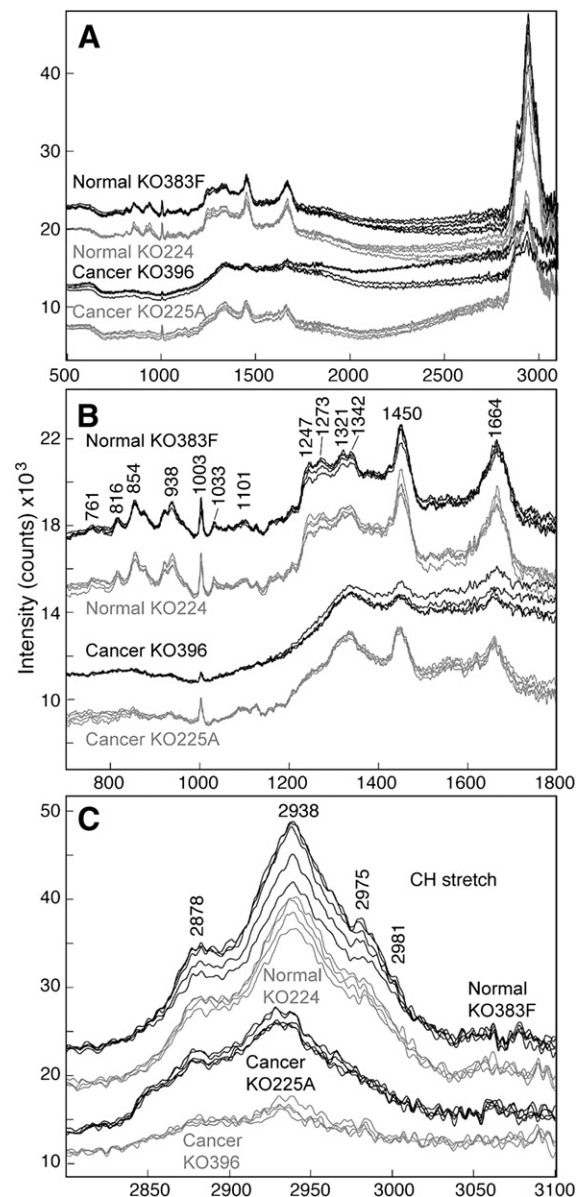


Figure 4. The as-recorded Raman spectra of normal cervical squamous cells and invasive cervical cancer cells (A). Details of these Raman spectra are enlarged for display in (B) the fingerprint region of 700 to 1800 cm^{-1} and (C) the high-wavenumber region of 2800 to 3100 cm^{-1} . Reprinted with permission.⁴³ Copyright 2010 Society for Applied Spectroscopy.

normal and cancerous colonic tissues were generated using Raman spectra of individual tissue constituents, including proteins, lipids, collagen, nucleic acid, and mucus. These Raman maps were shown to correlate with hematoxylin and eosin (H&E) stains, demonstrating the use of proteins and nucleic acids as potential spectroscopic biomarkers for the differentiation of adenocarcinomatous tissues.

Laser tweezers Raman spectroscopy (LTRS) has also been investigated for single-cell colorectal cancer diagnosis.⁵² At the early stages of colon cancer development, the epithelium layer on the luminal surface carries diagnostic information whereas the

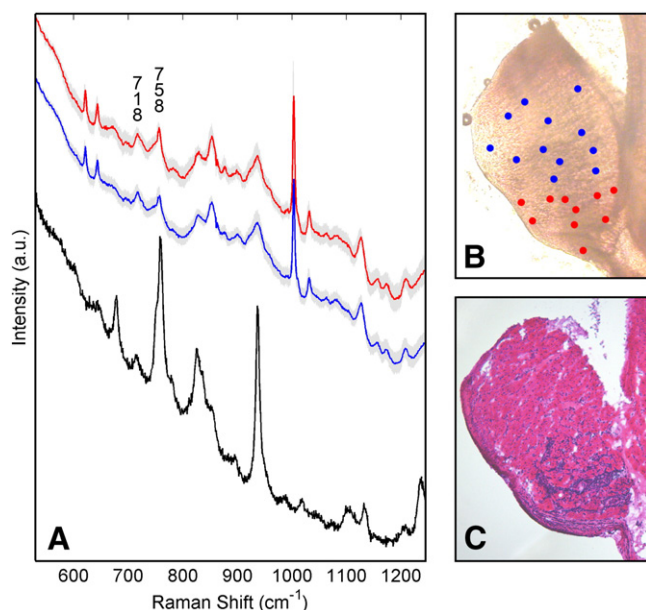


Figure 5. A grade 1R (mild rejection) endomyocardial biopsy sample is examined by Raman spectroscopy (A), optical microscope (B), and histopathology (C). Raman spectra are collected at locations marked in Figure 1, B. Rejected Raman spectra ($I_{758} > I_{718}$) and their corresponding locations are marked in red, and the normal spectra ($I_{758} < I_{718}$) in blue. The averages of normal and rejected spectra are plotted in Figure 1, A, with the spectrum of rejection biomarker serotonin in black. The shaded area around the averaged spectra equals ± 1 standard deviation. The H&E-stained image of an adjacent tissue section is shown in Figure 1, C. The distribution of rejected Raman spectra matches that of lymphocytes, and the distribution of normal Raman spectra matches that of normal cardiac muscle. Reprinted with permission.⁵⁴ Copyright 2009 John Wiley and Sons.

underlying bulk tissues are mostly irrelevant. To minimize the fluorescence background from the bulk tissues, laser tweezers are used to trap single cells from the epithelium and inspect them in isolation using Raman spectroscopy. Sensitivity of 86.3% and specificity of 86.3% have been reported with laser tweezers Raman spectroscopy.⁵³

Allograft rejection

Allograft transplantation is the last-resort therapy for patients with failed organs. Its efficacy relies on the successful management of the recipient's immune responses. Several studies using Raman spectroscopy to detect acute allograft rejection after transplantation have shown promising results.^{54–56} Chang and colleagues have examined the use of Raman spectroscopy for cardiac allograft rejection surveillance.⁵⁴ The diagnostic results using Raman spectroscopy were compared with H&E-stained images of graded endomyocardial biopsy tissues (Figure 5, B, C). The distribution of rejected Raman spectra on the biopsy tissue matches that of lymphocytes, and the distribution of normal Raman spectra matches that of normal cardiac muscle. PCA was applied to confirm and visualize the Raman diagnostic results. A specific biomarker, serotonin, was identified and used to improve differentiability.

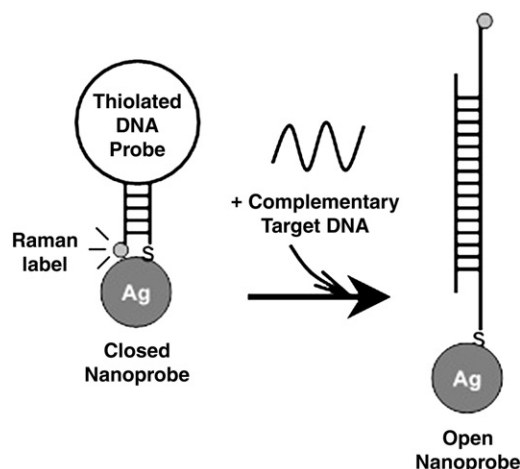


Figure 6. SERS-based molecular sentinel (MS) nanoprobe. The MS nanoprobe shown on the left of the figure is in the closed state and generates a strong SERS signal due to the proximity between the Raman label and the silver nanoparticle. In the presence of the complementary target DNA, the MS nanoprobe switches to the open state as shown on the right of the figure, and the SERS signal is significantly reduced due to the separation of the Raman label from the silver nanoparticle. Reprinted with permission.⁹ Copyright 2009 IOP Publishing.

Raman spectroscopy has also been used to detect acute rejection after renal transplantation. Acute rejection typically occurs in 15–20% of the patients within the first year of renal transplant, and currently the most commonly used diagnostic indicator is serum creatinine elevation. However, this method has been shown to have low sensitivity and specificity, because serum creatinine level can be affected by other disease conditions. In addition, serum creatinine level elevates only after significant histological damages have already taken place.⁵⁵ Using Raman spectroscopy, Brown et al observed significant spectral differences between activated and naive T lymphocytes, and reported a sensitivity and specificity of 95.7% and 100%, respectively.⁵⁶ This result demonstrates the potential of Raman spectroscopy as a minimally invasive screening tool for acute renal transplantation rejection.

SERS for biomarkers

SERS has been used to detect various biomolecules and proteins, such as glucose, hemoglobins, RNAs, and pathogens.^{57–60} Detection using SERS is especially advantageous for small signaling molecules that often lack recognizable epitopes for antibody-based immunohistochemistry. For instance, immunohistochemical detection of serotonin, an important immunomodulator involved in various immune-related diseases such as cardiac allograft rejection, rheumatoid arthritis,⁶¹ and HIV,^{62,63} has been largely limited by its small molecule size (~ 200 Da) and the resultant uncertainty in antibody specificity.⁶⁴ In a recent study using SERS, serotonin was quantitatively detected against a background of various other indolic molecules, including tryptophan, melatonin, and 5-hydroxyindoleacetic acid.⁶⁵ The relationship between surface enhancement factors, pH levels, and color changes of the solution was also examined. In another SERS study, Huang and

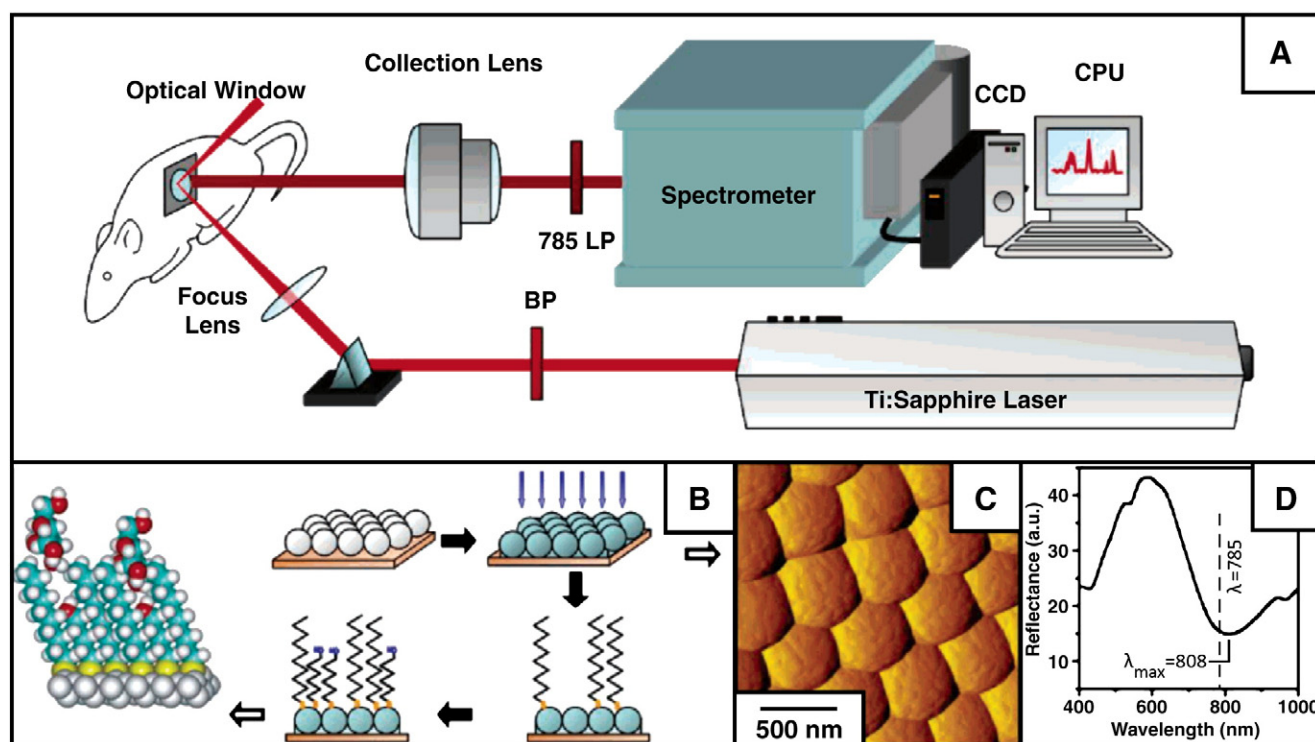


Figure 7. In vivo glucose detection using SERS. A rat with a surgically implanted sensor and optical window was examined by a conventional laboratory Raman spectroscopy system (A). The SERS-based sensor was fabricated using silver films over nanosphere (B). The resultant nanostructure (C) is shown using an atomic force microscope. After functionalization, a reflectance spectrum (D) was collected to determine the position of the localized surface plasmon resonance. BP, band-pass filter; CCD, charge-coupled device; CPU, computer processing unit; LP, low-pass filter. Reprinted with permission.⁷⁵ Copyright 2006 American Chemical Society.

co-workers conjugated gold nanorods to antibodies specific to epidermal growth factor receptor and demonstrated its use as a potential cancer diagnostic tool.⁶⁶ Because of the large curvatures, gold nanorods in theory have the strongest surface electromagnetic field compared with other colloid shapes.⁶⁷ In this study, gold nanorods were coated with poly(styrene sulfonate) to stabilize the colloids and to reverse the surface charge polarity from negative to positive for antibody conjugation. Minimal Raman signals were observed on normal cells, whereas significantly stronger Raman signals were detected on cancer cells, demonstrating specific antibody binding. The detection specificity was provided by the antibody, and the SERS signal served simply as the readout. Other novel SERS-based techniques such as nanoprobe technology have also been developed.^{9,68,69} As an example, the molecular sentinel (MS) nanoprobe consisted of a DNA hairpin probe with one end binding to a silver nanoparticle and the other tagged with a SERS signal reporter. In the absence of the target DNA, significant SERS signals were observed, because the SERS signal reporter was close enough to the silver nanoparticle on the other end of the folded stem-loop structure (Figure 6, left). While in the presence of the complementary target DNA, the SERS signal was significantly reduced as a result of the semiloop unfolding and separation of the SERS signal reporter from the silver nanoparticle (Figure 6, right). Multiplexing was achieved by mixing two MS nanoprobe specific to the breast cancer biomarker genes, *ERBB2*

and *MKI67*, to simultaneously detect both target DNAs present in the sample.

SERS for in vivo detection

The application of SERS for in vivo diagnostics in complex living systems is a challenging task. The surface of the nanoparticle must be biocompatible and placed in vivo without causing damage to the living system. In addition, the in vivo environments are awash with a variety of molecules and contaminants that may deactivate the SERS surface or interfere with the Raman signals of interest. Moreover, the concentrations of all molecules, both targets and contaminants, are constantly changing. Recently several successful in vivo SERS experiments have been demonstrated.^{70–74} Stuart and colleagues performed in vivo SERS on rats and quantitatively determined glucose concentration in the interstitial fluid.⁷⁵ The SERS-based sensor was fabricated using silver films over nanospheres (Figure 7, B). Hydrophilic pockets were formed around the sensor and partitioned glucose to the SERS-active surface, while excluding other molecules in the interstitial fluid such as plasma proteins. A glass window was surgically placed on the rat, allowing the sensor to be in contact with interstitial fluid and optically accessible for Raman spectroscopy (Figure 7, A). In their more recent work,⁷⁶ the window was removed and SERS spectra were collected transcutaneously. To obtain Raman signals deeper in the tissues, spatially offset Raman spectroscopy was applied, in

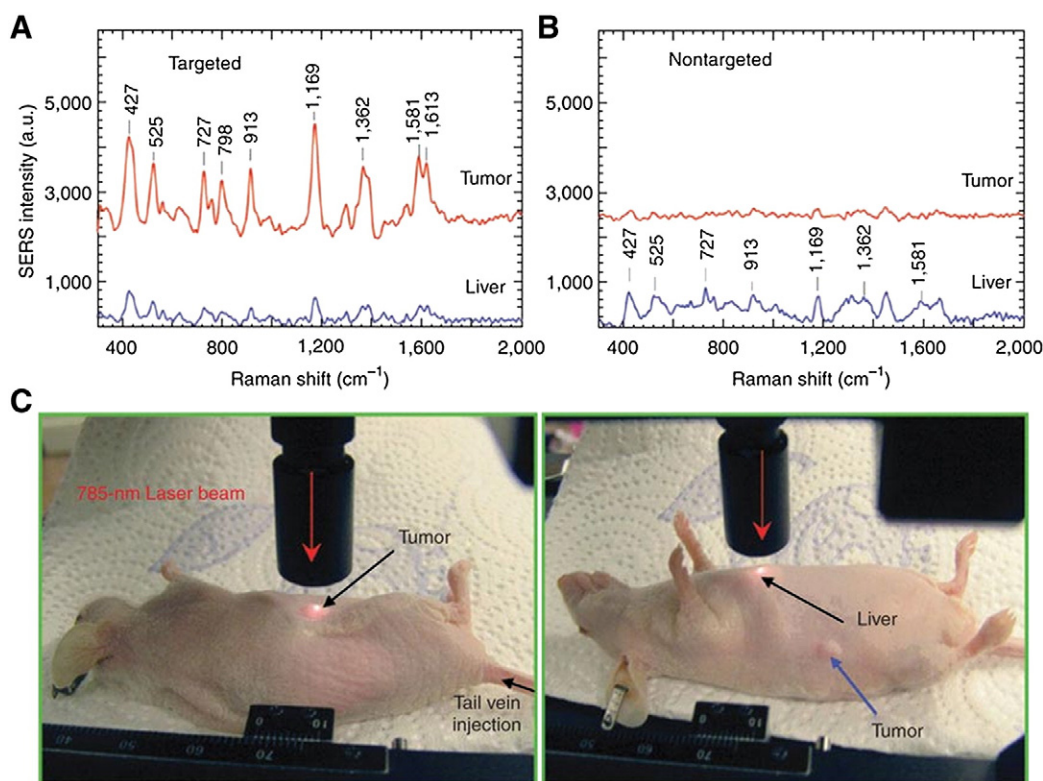


Figure 8. In vivo SERS detection of tumor biomarker EGFR using single-chain variable fragment antibody–conjugated gold nanoparticles. The bottom panels show the experimental setup. The top panels show spectra obtained from the tumor (red) and the liver (blue) by using targeted (A) and nontargeted (B) nanoparticles. In vivo SERS spectra were clearly observed from the tumor site using targeted nanoparticles, but not with nontargeted nanoparticles. Reprinted by permission from Macmillan Publishers Ltd. Nature Nanotechnology, copyright 2007.¹⁰

which the Raman scattered light was collected with a spatial offset from the point of laser incidence.^{77,78} In another recent study, Qian and co-workers demonstrated in vivo tumor detection using SERS with PEGylated gold nanoparticles.¹⁰ The SERS sensor was prepared by binding the reporter molecule diethylthiatri-carbocyanine to the gold colloids. A mixture of thiol-PEG and a heterofunctional PEG (SH-PEG-COOH) was then coated to stabilize the gold colloid–diethylthiatri-carbocyanine complex. Cancer cell–specific single-chain variable fragment B10 antibodies were conjugated at the last step. As shown in Figure 8, C, the sensor was injected through the tail vein into the mice bearing human head-and-neck tumors. Highly resolved SERS signals were observed specifically at the tumor site (Figure 8, A, B). Keren's group demonstrated in vivo Raman imaging in a similar study using single-walled carbon nanotubes (SWNTs).⁷⁹ As SWNTs inherently exhibit a strong Raman peak at 1593 cm^{-1} , Raman imaging using SWNTs does not rely on SERS reporter molecules and therefore requires fewer conjugation processes.

Emerging techniques of Raman spectroscopy

Single-walled carbon nanotubes

SWNTs are a useful diagnostic tool in nanomedicine.^{3,80–83} It has been shown that conjugation to SWNTs improves the permeability, as well as enhances the retention, of various functional moieties in the tumor tissues.^{84,85} This enhanced

permeability and retention effect of SWNTs has been explored for drug delivery where various biomolecules such as chemotherapeutic agents, proteins, and DNA were conjugated to SWNTs and delivered to tumor sites.^{86–89} SWNTs' intrinsic Raman peak at 1593 cm^{-1} (G-band) is typically used as the unambiguous marker to detect SWNT conjugates in drug delivery and Raman imaging studies.^{90–93} In an in vivo cancer drug delivery study, paclitaxel, a chemotherapy drug, was conjugated to SWNTs and injected into mice.⁸⁸ Raman spectroscopy was used to quantify the pharmacokinetics and biodistribution of this SWNT–paclitaxel conjugate without any radio or fluorescent label. Raman imaging is another area where SWNTs find important applications.^{79,91} Zavaleta and co-workers have shown noninvasive Raman imaging of tumors on mice in vivo using SWNTs.⁹¹ The SWNTs were linked to arginine-glycine-aspartic acid (RGD) peptides, which specifically target integrin $\alpha_v\beta_3$, an integrin overexpressed in angiogenic vessels and various tumor cells. After subcutaneous injection of this SWNT–RGD conjugate, in vivo Raman images of tumor were obtained using SWNTs' G-band intensity. In a more recent study, Liu et al successfully performed multicolor Raman imaging of living cells by multiplexing different isotope compositions.⁹⁴ SWNTs made of carbon-12 (^{12}C), carbon-13 (^{13}C), and $^{12}\text{C}/^{13}\text{C}$ mix were used, and each presented different G-band peak positions at 1590 , 1528 , and 1544 cm^{-1} , respectively. These three types of SWNTs were conjugated to the monoclonal antibody trastuzumab, marketed as Herceptin,

the monoclonal antibody cetuximab, marketed as Erbitux, and RGD peptides, recognizing Her2/neu, Her1/EGFR, and integrin $\alpha_v\beta_3$ cell surface receptors, respectively. These SWNT conjugates were then administered in vitro, and after incubation, multiplexed three-color Raman images were obtained, clearly identifying the existence of the three targeted cell receptors. Note that G-band spectral positions are key to distinguishing the three multiplexed colors in Raman imaging, and it was recently shown that up to five different colors could be achieved by varying the $^{12}\text{C}/^{13}\text{C}$ ratios in SWNTs.⁹⁵

Multiplexed SERS imaging

Multiplexed Raman imaging is capable of detecting multiple targets simultaneously, and it has attracted great interest recently.^{96–99} Gold nanoparticles are typically used as the tag in multiplexed SERS imaging for their narrow and strong SERS bands. In addition, silica-coated gold nanoparticles are biocompatible and nontoxic. In a recent work, Zavaleta et al achieved five-color multiplexed Raman imaging in vivo using five SERS nanotags adsorbed on gold nanoparticles.¹⁰⁰ Each nanotag generated a unique Raman signal, which is used as a multiplexed channel and assigned an arbitrary color in the resultant image. These five types of nanotagged gold nanoparticles were simultaneously injected through the tail vein and accumulated in the liver where a multiplexed five-color Raman image was obtained.

Using functionalized silver nanoparticles, Kennedy and co-workers demonstrated multiplexed SERS imaging of cell surface proteins in vitro.¹⁰¹ SERS signals from four differently functionalized nanoparticles were separated using least square fitting, and the spatial co-localization between the targeted proteins was visualized in the multiplexed SERS image. Other in vitro multiplexed SERS imaging works include cancer cell line identification where specific nanotags were used to recognize their respective biomarkers found on cancer cells.¹⁰²

Photothermal effect

Photothermal effect is an important feature of metal nanoparticles. The exposure of metal nanoparticles to laser induces an increase in temperature.²⁰ Application of this laser-induced thermal effect in Raman spectroscopy has recently been demonstrated, where plasmon heating was used to produce SERS-active microspots on colloidal crystals.¹⁰³ Polystyrene colloidal nanospheres were first coated with a 10-nm layer of gold nanoparticles and then with a 50-nm layer of amorphous TiO_2 deposited by atomic layer deposition. The resulting polystyrene-Au- TiO_2 core-shell nanospheres are assembled as colloidal crystals. When irradiated by a laser beam, the gold interlayer was strongly absorbing and the heat generated decomposed the polymeric spheres. A bowl-like pit was formed as a result, and the SERS effect of methylene blue adsorbed on these spots was demonstrated.

Core-shell nanoparticle structure for improved SERS reproducibility

Strong signal enhancement, high reproducibility, and stability are critical for effective SERS phenomena.¹⁰⁴ SERS studies using metal nanoparticles typically suffer from the desorption of Raman labels or target molecules from the metal surface, and the interference from the environment such as nontarget molecules and other surrounding metal nanoparticles. A core-shell structure

offers an effective solution to those stochastic interventions, in that the shell encapsulates the Raman labels or target molecules around the metal core and prevents the adsorption of other molecules as well as the aggregation of nanoparticles themselves. Various shell materials have been investigated, including polymers, silica, and metal.^{10,105–108} Among them, the stability and biocompatibility of silica makes it an attractive choice in medical research. Li and co-workers have developed ultrathin silica-coated gold nanoparticles with strong SERS signal and minimal gold aggregations.¹⁰⁵ Using etching technology, Roca's group developed silica-void-gold nanoparticles to prevent aggregations while allowing molecules to diffuse through the porous silica membranes and interact with the entrapped gold core.¹⁰⁹ In a more recent study Lim et al have demonstrated gold core-shell nanoparticles with highly uniform and reproducible SERS signals.¹¹⁰ The Raman labels trapped within the gap generated strong and highly quantitative SERS signals with 633-nm laser excitation. The development of new nanoparticles continues to expand the application of Raman spectroscopy in biology and medicine.

Analysis methods

Raman spectra obtained from biological samples often contain significant amounts of fluorescence background. As Raman spectral differences between normal and diseased tissues are generally subtle, effective data-processing algorithms are often required for data analysis and interpretation.

Fluorescence background removal

As mentioned above, Raman spectra collected from tissues are composed mainly of Raman scattering and intrinsic tissue fluorescence. To eliminate the fluorescence background, a polynomial function that fits to the fluorescence profile is usually subtracted from the Raman spectra.^{30,111–113} Although there is no consensus on the optimal order of the polynomial function, fourth- and fifth-order polynomials are most commonly employed.^{65,113–116}

Multivariate data analysis

Raman spectra contain various overlapping Raman bands. As a result, it is difficult to visually inspect and interpret the spectral data. Multivariate spectral analysis methods are often used to process the Raman spectra and facilitate data interpretation. Spectral analysis methods are generally categorized as either supervised or unsupervised. For unsupervised analyses, such as cluster analysis and PCA, no a priori knowledge of class characteristics is required but is to be determined from the analysis itself. In contrast, in a supervised analysis the number of classes and representative samples of each class are known a priori, as is the case in LDA, regression analysis, and artificial neural networks (ANNs).¹¹⁷ Several commonly used analysis methods are introduced below.

Hierarchical clustering

Hierarchical clustering is a cluster analysis method in which Raman spectra are grouped according to their similarities defined by the distance matrices. A distance matrix measures

dissimilarity among a group of objects—Raman spectra in this case. For example, the most commonly used distance metric is the euclidean distance, wherein a Raman spectrum with wavenumbers is expressed as $\mathbf{x} = [x_1, x_2, \dots, x_p]$, and the distance between two Raman spectra \mathbf{x}_i and \mathbf{x}_j is defined as

$$d_{ij} = \|\mathbf{x}_i - \mathbf{x}_j\| = \left[\sum_{k=1}^p (x_{ik} - x_{jk})^2 \right]^{\frac{1}{2}}$$

The clustering process is repeated at different levels to produce a tree structure, called the dendrogram, and the spectra from normal and diseased samples are discriminated at the end of the process. Hierarchical clustering is widely used in analytical Raman spectroscopy.^{25,35}

Principal component analysis

PCA is one of the most commonly used unsupervised classification methods in Raman spectroscopy. Raman spectra contain intensity information obtained at a large number of different wavenumbers. Each of these wavenumbers can be regarded as an independent dimension, on which the Raman spectral data are measured. PCA reduces the dimensionality of the original Raman data set, with most of its variance retained in the selected principal components.^{26,32,50,111,114,118,119} PCA has been successfully used in multivariate Raman spectral analysis and is widely accepted for data interpretation. A brief overview of PCA is provided below for a typical diagnostic Raman spectral data classification process.

The set of Raman spectra obtained from a diagnostic experiment can be expressed as an m by n matrix \mathbf{X} ,

$$\mathbf{X} = \begin{bmatrix} x_{11} & x_{12} & x_{13} & \cdots & x_{1n} \\ x_{21} & x_{22} & x_{23} & \cdots & x_{2n} \\ x_{31} & x_{32} & x_{33} & \cdots & x_{3n} \\ \vdots & \vdots & \vdots & \ddots & \vdots \\ x_{m1} & x_{m2} & x_{m3} & \cdots & x_{mn} \end{bmatrix} = [\mathbf{x}_1 \ \mathbf{x}_2 \ \mathbf{x}_3 \ \cdots \ \mathbf{x}_n],$$

where n is the number of Raman spectra taken in the experiment, m is the total number of spectral wavenumbers, and \mathbf{x}_i is a column vector of length m representing the i^{th} Raman spectrum. The covariance matrix \mathbf{C}_X of the original Raman data set \mathbf{X} can then be determined, as well as the eigenvectors of \mathbf{C}_X . The resulting eigenvector matrix \mathbf{W} is given by

$$\mathbf{W} = [\mathbf{w}_1 \ \mathbf{w}_2 \ \mathbf{w}_3 \ \cdots \ \mathbf{w}_m],$$

where \mathbf{w}_i is a column vector of length m representing the i^{th} eigenvector of \mathbf{C}_X . Note that the eigenvectors are arranged with descending eigenvalues—that is, decreasing contributions to the overall variance of the Raman data set.

The principal component score \mathbf{P} is obtained by projecting the original Raman data set \mathbf{X} onto the new basis spanned by the eigenvectors, that is,

$$\mathbf{P} = \mathbf{W}^T \mathbf{X} = [\mathbf{p}_1 \ \mathbf{p}_2 \ \mathbf{p}_3 \ \cdots \ \mathbf{p}_m],$$

where \mathbf{p}_i is a column vector of length n representing the scores of the i^{th} principal component for each of the n measurements in

the Raman data set. As the principal components corresponding to the largest eigenvalues account for most of the variations in the data set, classification of Raman spectra in most cases can be achieved with these first few principal components. PCA is therefore a powerful analytical tool for dimensionality reduction in Raman spectroscopy.

Linear discriminant analysis

LDA is another commonly used spectral data classification method. As the projection axes produced by PCA do not always provide clear boundaries for between-class discrimination, LDA is often used to improve the class separation following PCA. One of the most common LDA approaches is Fisher's criterion. It is a supervised analysis that maximizes the between-class variance while minimizing the within-class variance in a set of Raman spectra. Effective class separation is achieved by projecting the Raman data into a new eigenvector set.^{34,49,114,120,121} This method applied to a two-class problem is briefly described below.

Within-class and between-class scatter matrices are used to formulate the criterion. The within-class scatter matrix is defined as

$$\mathbf{S}_W = \sum_{i=1,2} \sum_{\mathbf{x} \in C_i} (\mathbf{x} - \mathbf{m}_i)(\mathbf{x} - \mathbf{m}_i)^T,$$

where \mathbf{x} is a column vector representing an individual Raman spectrum in class C_i , and \mathbf{m}_i is the mean of the Raman spectra in class C_i , $i = 1, 2$. The between-class scatter matrix is given by $\mathbf{S}_B = (\mathbf{m}_1 - \mathbf{m}_2)(\mathbf{m}_1 - \mathbf{m}_2)^T$, where \mathbf{m}_1 and \mathbf{m}_2 are defined above. The Fisher's criterion function,

$$J(\mathbf{w}) = \frac{\mathbf{w}^T \mathbf{S}_B \mathbf{w}}{\mathbf{w}^T \mathbf{S}_W \mathbf{w}},$$

is used to evaluate the classification. A vector \mathbf{w} that maximizes the function $J(\mathbf{w})$ is the solution to the generalized eigenvalue problem $\mathbf{S}_B \mathbf{w} = \lambda \mathbf{S}_W \mathbf{w}$. The eigenvector \mathbf{w} is then used as the new basis vector. Once the data set is transformed onto this vector, euclidean distance can be used for data classification. However, some data located in the middle of the two classes might not be easily categorized.

Artificial neural network

Whereas LDA can discriminate only classes that are linearly separable, ANN is a nonlinear method capable of multidimensional bounding problems. ANN emulates the process of the human mind by employing artificial neuron functions in which each neuron provides an output value based on multiple inputs. Typically, an ANN consists of multiple layers, including the input layer, the hidden layer, and the output layer. Neurons on the input layer take the Raman spectral data as inputs, and the classifications are made at the output layer. Each neuron in the hidden layers sums up the inputs from neurons in preceding layers with certain weights. These "middle" neurons then send out their outputs after some nonlinear operations, such as hyperbolic tangents, step functions, and sigmoid functions. The weights are computed using a set of known data during the training process. The number of hidden layers, the neuron functions, and the form of the data are crucial parameters for an effective ANN design.¹²² Note that which Raman spectral

features to be used as inputs should be carefully chosen for optimal classification. One example of Raman spectral analysis using ANN is the single-cell diagnosis of colorectal cancer.⁵³

Ordinary least squares regression

Ordinary least squares (OLS) is a commonly used linear regression method that minimizes the sum of squared distances between experimental data and the corresponding fitted curve. OLS is often used to determine the compositional concentrations of a tissue sample, where the sample spectrum is fitted to the individual composition's Raman spectra and a weighted sum is obtained from the fitting coefficients.^{8,25} Briefly, the Raman spectrum of a tissue sample (or solution mixture) can be expressed as an $m \times 1$ column vector $\mathbf{y} = [y_1 \ y_2 \ y_3 \ \dots \ y_m]^T$, where m is the number of wavenumbers at which Raman shifts are recorded. Similarly, Raman spectra of its component chemicals can be expressed as column vectors and put together as an $m \times n$ matrix \mathbf{Z} ,

$$\mathbf{Z} = \begin{bmatrix} z_{11} & z_{12} & z_{13} & \cdots & z_{1n} \\ z_{21} & z_{22} & z_{23} & \cdots & z_{2n} \\ z_{31} & z_{32} & z_{33} & \cdots & z_{3n} \\ \vdots & \vdots & \vdots & \ddots & \vdots \\ z_{m1} & z_{m2} & z_{m3} & \cdots & z_{mn} \end{bmatrix},$$

where n is the number of component chemicals, and m is the same set of wavenumbers as defined above. The OLS coefficient $\boldsymbol{\beta} = [\beta_1 \ \beta_2 \ \beta_3 \ \dots \ \beta_n]^T$ needs to satisfy $\mathbf{y} = \mathbf{Z}\boldsymbol{\beta} + \mathbf{u}$, where \mathbf{u} is an $m \times 1$ error vector. OLS minimizes the residual sum of squares $SSR = |\mathbf{y} - \mathbf{Z}\boldsymbol{\beta}|^2 = (\mathbf{y} - \mathbf{Z}\boldsymbol{\beta})^T (\mathbf{y} - \mathbf{Z}\boldsymbol{\beta})$ by setting the derivative of SSR with respect to $\boldsymbol{\beta}$ equal to 0. The OLS estimator $\boldsymbol{\beta}$ is then calculated to be $\boldsymbol{\beta} = (\mathbf{Z}^T \mathbf{Z})^{-1} \mathbf{Z}^T \mathbf{y}$.¹²³ Considering that the weights of components are positive, a nonnegativity constraint is applied in this case to avoid negative fitting coefficients, and this variant of OLS is called nonnegative least squares.

Raman spectroscopy is a powerful analytical tool, and it has been successfully used in various biomedical applications. Its clinical potential, both in vivo and in vitro, has also been demonstrated for various diseases. An overview of current Raman spectroscopic applications and associated experimental and analysis techniques is presented here to facilitate a wider adoption of Raman spectroscopy in both biomedical and clinical laboratories.

Appendix A. Supplementary data

Supplementary data to this article can be found online at doi:10.1016/j.nano.2011.09.013.

References

- Mansour HM, Hickey AJ. Raman characterization and chemical imaging of biocolloidal self-assemblies, drug delivery systems, and pulmonary inhalation aerosols: a review. *AAPS PharmSciTech* 2007;8:E99.
- Lopez T, Ortiz E, Alvarez M, Navarrete J, Odriozola JA, Martinez-Ortega F, et al. Study of the stabilization of zinc phthalocyanine in sol-gel TiO₂ for photodynamic therapy applications. *Nanomed Nanotechnol Biol Med* 2010;6:777-85.
- Biris AS, Galanzha EI, Li Z, Mahmood M, Xu Y, Zharov VP. In vivo Raman flow cytometry for real-time detection of carbon nanotube kinetics in lymph, blood, and tissues. *J Biomed Opt* 2009;021006:14.
- Liu Z, Davis C, Cai W, He L, Chen X, Dai H. Circulation and long-term fate of functionalized, biocompatible single-walled carbon nanotubes in mice probed by Raman spectroscopy. *Proc Natl Acad Sci U S A* 2008;105:1410-5.
- Nakajima H, Ozaki K, Hongyo T, Narama I, Todo T. A rapid and easy method for the qualitative detection of intracellular deposition of inhaled nanoparticles. *Nanomed Nanotechnol Biol Med* 2011, doi:10.1016/j.nano.2011.02.004 (published online 1 March).
- Crow P, Stone N, Kendall CA, Uff JS, Farmer JA, Barr H, et al. The use of Raman spectroscopy to identify and grade prostatic adenocarcinoma in vitro. *Br J Cancer* 2003;89:106-8.
- Rehman S, Movasaghi Z, Tucker AT, Joel SP, Darr JA, Ruban AV, et al. Raman spectroscopic analysis of breast cancer tissues: identifying differences between normal, invasive ductal carcinoma and ductal carcinoma in situ of the breast tissue. *J Raman Spectrosc* 2007;38:1345-51.
- Haka AS, Shafer-Peltier KE, Fitzmaurice M, Crowe J, Dasari RR, Feld MS. Diagnosing breast cancer by using Raman spectroscopy. *Proc Natl Acad Sci U S A* 2005;102:12371-6.
- Wang HN, Vo-Dinh T. Multiplex detection of breast cancer biomarkers using plasmonic molecular sentinel nanoprobe. *Nanotechnology* 2009;065101:20.
- Qian X, Peng XH, Ansari DO, Yin-Goen Q, Chen GZ, Shin DM, et al. In vivo tumor targeting and spectroscopic detection with surface-enhanced Raman nanoparticle tags. *Nat Biotechnol* 2008;26:83-90.
- Chen Z, Tabakman SM, Goodwin AP, Kattah MG, Daranciang D, Wang X, et al. Protein microarrays with carbon nanotubes as multicolor Raman labels. *Nat Biotechnol* 2008;26:1285-92.
- Wang X, Qian X, Beitler JJ, Chen ZG, Khuri FR, Lewis MM, et al. Detection of circulating tumor cells in human peripheral blood using surface-enhanced Raman scattering nanoparticles. *Cancer Res* 2011;71:1526-32.
- E. Smith, G. Dent, *Modern Raman spectroscopy: a practical approach*. Hoboken, NJ: Wiley; 2005. p. 1-5, 71-3.
- Gremlich HU, Yan B. *Infrared and Raman spectroscopy of biological materials*. New York: M. Dekker; 2001.
- Le Ru EC, Blackie E, Meyer M, Etchegoin PG. Surface-enhanced Raman scattering enhancement factors: a comprehensive study. *J Phys Chem C* 2007;111:13794-803.
- Park WH, Kim ZH. Charge transfer enhancement in the SERS of a single molecule. *Nano Lett* 2010;10:4040-8.
- Fang Y, Seong NH, Dlott DD. Measurement of the distribution of site enhancements in surface-enhanced Raman scattering. *Science* 2008;321:388-92.
- Stiles PL, Dieringer JA, Shah NC, Van Duyne RP. Surface-enhanced Raman spectroscopy. *Annu Rev Anal Chem* 2008;1:601-26.
- Campion A, Kambhampati P. Surface-enhanced Raman scattering. *Chem Soc Rev* 1998;27:241-50.
- Lu X, Rycenga M, Skrabalak SE, Wiley B, Xia Y. Chemical synthesis of novel plasmonic nanoparticles. *Annu Rev Phys Chem* 2009;60:167-92.
- Link S, El-Sayed MA. Optical properties and ultrafast dynamics of metallic nanocrystals. *Annu Rev Phys Chem* 2003;54:331-66.
- Kho KW, Shen ZX, Lei Z, Watt F, Soo KC, Olivo M. Investigation into a surface plasmon-related heating effect in surface-enhanced Raman spectroscopy. *Anal Chem* 2007;79:8870-82.
- American Cancer Society. *Cancer Facts & Figures*. Atlanta: American Cancer Society; 2010.
- Haka AS, Volynskaya Z, Gardecki JA, Nazemi J, Shenk R, Wang N, et al. Diagnosing breast cancer using Raman spectroscopy: prospective analysis. *J Biomed Opt* 2009;14:054023.
- de Jong BWD, Bakker TC, Maquelin K, van der Kwast T, Bangma CH, Kok DJ, et al. Discrimination between nontumor bladder tissue and tumor by Raman spectroscopy. *Anal Chem* 2006;78:7761-9.

26. Crow P, Barras B, Kendall C, Hart-Prieto M, Wright M, Persad R, et al. The use of Raman spectroscopy to differentiate between different prostatic adenocarcinoma cell lines. *Br J Cancer* 2005;92:2166–70.
27. Ghanate AD, Kothiwale S, Singh SP, Bertrand D, Krishna CM. Comparative evaluation of spectroscopic models using different multivariate statistical tools in a multicancer scenario. *J Biomed Opt* 2011;16:025003.
28. Oshima Y, Shinzawa H, Takenaka T, Furihata C, Sato H. Discrimination analysis of human lung cancer cells associated with histological type and malignancy using Raman spectroscopy. *J Biomed Opt* 2010;15:017009.
29. Teh SK, Zheng W, Ho KY, Teh M, Yeoh KG, Huang Z. Near-infrared Raman spectroscopy for early diagnosis and typing of adenocarcinoma in the stomach. *Br J Surg* 2011;97:550–7.
30. Matousek P, Stone N. Prospects for the diagnosis of breast cancer by noninvasive probing of calcifications using transmission Raman spectroscopy. *J Biomed Opt* 2007;12:024008.
31. Haka AS, Volynskaya Z, Gardecki JA, Nazemi J, Lyons J, Hicks D, et al. In vivo margin assessment during partial mastectomy breast surgery using Raman spectroscopy. *Cancer Res* 2006;66:3317–22.
32. Chowdary MV, Kumar KK, Kurien J, Mathew S, Krishna CM. Discrimination of normal, benign, and malignant breast tissues by Raman spectroscopy. *Biopolymers* 2006;83:556–69.
33. Keller MD, Vargis E, Granja NdM, Wilson RH, Mycek MA, Kelley MC, et al. Development of a spatially offset Raman spectroscopy probe for breast tumor surgical margin evaluation. *J Biomed Opt* 2011;077006:16.
34. Pichardo-Molina JL, Frausto-Reyes C, Barbosa-Garcia O, Huerta-Franco R, Gonzalez-Trujillo JL, Ramirez-Alvarado CA, et al. Raman spectroscopy and multivariate analysis of serum samples from breast cancer patients. *Lasers Med Sci* 2007;22:229–36.
35. Beljebbar A, Bouche O, Diebold MD, Guillou PJ, Palot JP, Eudes D, et al. Identification of Raman spectroscopic markers for the characterization of normal and adenocarcinomatous colonic tissues. *Crit Rev Oncol Hematol* 2009;72:255–64.
36. Kirsch M, Schackert G, Salzer R, Krafft C. Raman spectroscopic imaging for in vivo detection of cerebral brain metastases. *Anal Bioanal Chem* 2010;398:1707–13.
37. Draux F, Gobinet C, Sule-Suso J, Trussardi A, Manfait M, Jeannesson P, et al. Raman spectral imaging of single cancer cells: probing the impact of sample fixation methods. *Anal Bioanal Chem* 2010;397:2727–37.
38. Bonnier F, Knief P, Lim B, Meade AD, Dorney J, Bhattacharya K, et al. Imaging live cells grown on a three-dimensional collagen matrix using Raman microspectroscopy. *Analyst* 2010;135:3169–77.
39. Neugebauer U, Clement JH, Bocklitz T, Krafft C, Popp J. Identification and differentiation of single cells from peripheral blood by Raman spectroscopic imaging. *J Biophotonics* 2010;3:579–87.
40. Wu Y, McEwen GD, Harihar S, Baker SM, DeWald DB, Zhou A. BRMS1 expression alters the ultrastructural, biomechanical and biochemical properties of MDA-MB-435 human breast carcinoma cells: an AFM and Raman microspectroscopy study. *Cancer Lett* 2010;293:82–91.
41. Hartsuiker L, Zeijen NJ, Terstappen LW, Otto C. A comparison of breast cancer tumor cells with varying expression of the Her2/neu receptor by Raman microspectroscopic imaging. *Analyst* 2010;135:3220–6.
42. Mariani MM, Maccoux LJ, Mattheus C, Diem M, Hengstler JG, Deckert V. Micro-Raman detection of nuclear membrane lipid fluctuations in senescent epithelial breast cancer cells. *Anal Chem* 2010;82:4259–63.
43. Kamemoto LE, Misra AK, Sharma SK, Goodman MT, Luk H, Dykes AC, et al. Near-infrared micro-Raman spectroscopy for in vitro detection of cervical cancer. *Appl Spectrosc* 2010;64:255–61.
44. Mayrand MH, Duarte-Franco E, Rodrigues I, Walter SD, Hanley J, Ferenczy A, et al. Human papillomavirus DNA versus Papanicolaou screening tests for cervical cancer. *N Engl J Med* 2007;357:1579–88.
45. Robichaux-Viehoever A, Kanter E, Shappell H, Billheimer D, Jones III H, Mahadevan-Jansen A. Characterization of Raman spectra measured in vivo for the detection of cervical dysplasia. *Appl Spectrosc* 2007;61:986–93.
46. Utzinger U, Richards-Kortum RR. Fiber optic probes for biomedical optical spectroscopy. *J Biomed Opt* 2003;8:121–47.
47. Kanter EM, Majumder S, Vargis E, Robichaux-Viehoever A, Kanter GJ, Shappell H, et al. Multiclass discrimination of cervical precancers using Raman spectroscopy. *J Raman Spectrosc* 2009;40:205–11.
48. Kanter EM, Vargis E, Majumder S, Keller MD, Woeste E, Rao GG, et al. Application of Raman spectroscopy for cervical dysplasia diagnosis. *J Biophotonics* 2009;2:81–90.
49. Mo J, Zheng W, Low JJ, Ng J, Ilancheran A, Huang Z. High wavenumber Raman spectroscopy for in vivo detection of cervical dysplasia. *Anal Chem* 2009;81:8908–15.
50. Krishna CM, Prathima NB, Malini R, Vadhira BM, Bhatt RA, Fernandes DJ, et al. Raman spectroscopy studies for diagnosis of cancers in human uterine cervix. *Vib Spectrosc* 2006;41:136–41.
51. Widjaja E, Zheng W, Huang Z. Classification of colonic tissues using near-infrared Raman spectroscopy and support vector machines. *Int J Oncol* 2008;32:653–62.
52. Chen K, Qin Y, Zheng F, Sun M, Shi DR. Diagnosis of colorectal cancer using Raman spectroscopy of laser-trapped single living epithelial cells. *Opt Lett* 2006;31:2015–7.
53. Zheng F, Qin Y, Chen K. Sensitivity map of laser tweezers Raman spectroscopy for single-cell analysis of colorectal cancer. *J Biomed Opt* 2007;034002:12.
54. Chung YG, Tu Q, Cao D, Harada S, Eisen HJ, Chang C. Raman spectroscopy detects cardiac allograft rejection with molecular specificity. *Clin Transl Sci* 2009;2:206–10.
55. Brown KL, Palyvoda OY, Thakur JS, Nehlsen-Cannarella SL, Fagoaga OR, Gruber SA, et al. Differentiation of alloreactive versus CD3/CD28-stimulated T-lymphocytes using Raman spectroscopy: a greater specificity for noninvasive acute renal allograft rejection detection. *Cytometry A* 2009;75:917–23.
56. Brown KL, Palyvoda OY, Thakur JS, Nehlsen-Cannarella SL, Fagoaga OR, Gruber SA, et al. Raman spectroscopic differentiation of activated versus non-activated T lymphocytes: an in vitro study of an acute allograft rejection model. *J Immunol Methods* 2009;340:48–54.
57. Han XX, Huang GG, Zhao B, Ozaki Y. Label-free highly sensitive detection of proteins in aqueous solutions using surface-enhanced Raman scattering. *Anal Chem* 2009;81:3329–33.
58. Qian XM, Nie SM. Single-molecule and single-nanoparticle SERS: from fundamental mechanisms to biomedical applications. *Chem Soc Rev* 2008;37:912–20.
59. Kang T, Yoo SM, Yoon I, Lee SY, Kim B. Patterned multiplex pathogen DNA detection by Au particle-on-wire SERS sensor. *Nano Lett* 2010;10:1189–93.
60. Driskell JD, Seto AG, Jones LP, Jokela S, Dluhy RA, Zhao YP, et al. Rapid microRNA (miRNA) detection and classification via surface-enhanced Raman spectroscopy (SERS). *Biosens Bioelectron* 2008;24:923–8.
61. Kling A, Rantapaa-Dahlqvist S, Stenlund H, Mjorndal T. Decreased density of serotonin 5-HT_{2A} receptors in rheumatoid arthritis. *Ann Rheum Dis* 2006;65:816–9.
62. Maneglier B, Guillemin GJ, Clayette P, Rogez-Kreuz C, Brew BJ, Dormont D, et al. Serotonin decreases HIV-1 replication in primary cultures of human macrophages through 5-HT_{1A} receptors. *Br J Pharmacol* 2008;154:174–82.
63. Evans DL, Lynch KG, Benton T, Dube B, Gettes DR, Tustin NB, et al. Selective serotonin reuptake inhibitor and substance P antagonist enhancement of natural killer cell innate immunity in human immunodeficiency virus/acquired immunodeficiency syndrome. *Biol Psychiatry* 2008;63:899–905.
64. Gordon J, Barnes NM. Serotonin: a real blast for T cells. *Blood* 2007;109:3130–1.
65. Tu Q, Eisen J, Chang C. Surface-enhanced Raman spectroscopy study of indolic molecules adsorbed on gold colloids. *J Biomed Opt* 2010;020512:15.
66. Huang X, El-Sayed IH, Qian W, El-Sayed MA. Cancer cells assemble and align gold nanorods conjugated to antibodies to produce highly

- enhanced, sharp, and polarized surface Raman spectra: a potential cancer diagnostic marker. *Nano Lett* 2007;7:1591-7.
67. Hao E, Schatz GC. Electromagnetic fields around silver nanoparticles and dimers. *J Chem Phys* 2004;120:357-66.
68. Kneipp J, Kneipp H, Wittig B, Kneipp K. Novel optical nanosensors for probing and imaging live cells. *Nanomed Nanotechnol Biol Med* 2010;6:214-26.
69. Gregas MK, Yan F, Scaffidi J, Wang HN, Vo-Dinh T. Characterization of nanoprobe uptake in single cells: spatial and temporal tracking via SERS labeling and modulation of surface charge. *Nanomed Nanotechnol Biol Med* 2011;7:115-22.
70. Samanta A, Maiti KK, Soh KS, Liao X, Vendrell M, Dinis US, et al. Ultrasensitive near-infrared Raman reporters for SERS-based in vivo cancer detection. *Angew Chem Int Ed Engl* 2011;50:6089-92.
71. Bergholt MS, Zheng W, Lin K, Ho KY, Teh M, Yeoh KG, et al. Characterizing variability in in vivo Raman spectra of different anatomical locations in the upper gastrointestinal tract toward cancer detection. *J Biomed Opt* 2011;037003:16.
72. Mohs AM, Mancini MC, Singhal S, Provenziale JM, Leyland-Jones B, Wang MD, et al. Hand-held spectroscopic device for in vivo and intraoperative tumor detection: contrast enhancement, detection sensitivity, and tissue penetration. *Anal Chem* 2010;82:9058-65.
73. Maiti KK, Dinis US, Fu CY, Lee JJ, Soh KS, Yun SW, et al. Development of biocompatible SERS nanotag with increased stability by chemisorption of reporter molecule for in vivo cancer detection. *Biosens Bioelectron* 2010;26:398-403.
74. Qian J, Jiang L, Cai F, Wang D, He S. Fluorescence-surface enhanced Raman scattering co-functionalized gold nanorods as near-infrared probes for purely optical in vivo imaging. *Biomaterials* 2011;32:1601-10.
75. Stuart DA, Yuen JM, Shah N, Lyandres O, Yonzon CR, Glucksberg MR, et al. In vivo glucose measurement by surface-enhanced Raman spectroscopy. *Anal Chem* 2006;78:7211-5.
76. Yuen JM, Shah NC, Walsh Jr JT, Glucksberg MR, Van Duyne RP. Transcutaneous glucose sensing by surface-enhanced spatially offset Raman spectroscopy in a rat model. *Anal Chem* 2010;82:8382-5.
77. Matousek P, Clark IP, Draper ER, Morris MD, Goodship AE, Everall N, et al. Subsurface probing in diffusely scattering media using spatially offset Raman spectroscopy. *Appl Spectrosc* 2005;59:393-400.
78. Matousek P. Deep non-invasive Raman spectroscopy of living tissue and powders. *Chem Soc Rev* 2007;36:1292-304.
79. Keren S, Zavaleta C, Cheng Z, de la Zerda A, Gheysens O, Gambhir SS. Noninvasive molecular imaging of small living subjects using Raman spectroscopy. *Proc Natl Acad Sci U S A* 2008;105:5844-9.
80. Bhirde AA, Patel V, Gavard J, Zhang G, Sousa AA, Masedunskas A, et al. Targeted killing of cancer cells in vivo and in vitro with EGF-directed carbon nanotube-based drug delivery. *ACS Nano* 2009;3:307-16.
81. Liu Z, Tabakman S, Welsher K, Dai H. Carbon nanotubes in biology and medicine: in vitro and in vivo detection, imaging and drug delivery. *Nano Res* 2009;2:85-120.
82. Kostarelos K, Bianco A, Prato M. Promises, facts and challenges for carbon nanotubes in imaging and therapeutics. *Nat Nanotechnol* 2009;4:627-33.
83. De la Zerda A, Zavaleta C, Keren S, Vaithilingam S, Bodapati S, Liu Z, et al. Carbon nanotubes as photoacoustic molecular imaging agents in living mice. *Nat Nanotechnol* 2008;3:557-62.
84. Maeda H. The enhanced permeability and retention (EPR) effect in tumor vasculature: the key role of tumor-selective macromolecular drug targeting. *Adv Enzyme Regul* 2001;41:189-207.
85. Maeda H. Tumor-selective delivery of macromolecular drugs via the EPR effect: background and future prospects. *Bioconjug Chem* 2010;21:797-802.
86. Liu Z, Fan AC, Rakhra K, Sherlock S, Goodwin A, Chen X, et al. Supramolecular stacking of doxorubicin on carbon nanotubes for in vivo cancer therapy. *Angew Chem Int Ed Engl* 2009;48:7668-72.
87. Feazell RP, Nakayama-Ratchford N, Dai H, Lippard SJ. Soluble single-walled carbon nanotubes as longboat delivery systems for platinum(IV) anticancer drug design. *J Am Chem Soc* 2007;129:8438-9.
88. Liu Z, Chen K, Davis C, Sherlock S, Cao Q, Chen X, et al. Drug delivery with carbon nanotubes for in vivo cancer treatment. *Cancer Res* 2008;68:6652-60.
89. Kam NW, Liu Z, Dai H. Carbon nanotubes as intracellular transporters for proteins and DNA: an investigation of the uptake mechanism and pathway. *Angew Chem Int Ed Engl* 2006;45:577-81.
90. Xiao Y, Gao X, Taratula O, Treado S, Urbas A, Holbrook RD, et al. Anti-HER2 IgY antibody-functionalized single-walled carbon nanotubes for detection and selective destruction of breast cancer cells. *BMC Cancer* 2009;9:351.
91. Zavaleta C, de la Zerda A, Liu Z, Keren S, Cheng Z, Schipper M, et al. Noninvasive Raman spectroscopy in living mice for evaluation of tumor targeting with carbon nanotubes. *Nano Lett* 2008;8:2800-5.
92. Shi X, Wang SH, Shen M, Antwerp ME, Chen X, Li C, et al. Multifunctional dendrimer-modified multiwalled carbon nanotubes: synthesis, characterization, and in vitro cancer cell targeting and imaging. *Biomacromolecules* 2009;10:1744-50.
93. Welsher K, Liu Z, Sherlock SP, Robinson JT, Chen Z, Daranciang D, et al. A route to brightly fluorescent carbon nanotubes for near-infrared imaging in mice. *Nat Nanotechnol* 2009;4:773-80.
94. Liu Z, Li X, Tabakman SM, Jiang K, Fan S, Dai H. Multiplexed multicolor Raman imaging of live cells with isotopically modified single walled carbon nanotubes. *J Am Chem Soc* 2008;130:13540-1.
95. Liu Z, Tabakman S, Sherlock S, Li X, Chen Z, Jiang K, et al. Multiplexed five-color molecular imaging of cancer cells and tumor tissues with carbon nanotube Raman tags in the near-infrared. *Nano Res* 2010;3:222-33.
96. Kneipp J, Kneipp H, Rice WL, Kneipp K. Optical probes for biological applications based on surface-enhanced Raman scattering from indocyanine green on gold nanoparticles. *Anal Chem* 2005;77:2381-5.
97. Hu Q, Tay LL, Noestheden M, Pezacki JP. Mammalian cell surface imaging with nitrile-functionalized nanoprobe: biophysical characterization of aggregation and polarization anisotropy in SERS imaging. *J Am Chem Soc* 2007;129:14-5.
98. Matschulat A, Drescher D, Kneipp J. Surface-enhanced Raman scattering hybrid nanoprobe multiplexing and imaging in biological systems. *ACS Nano* 2010;4:3259-69.
99. Kneipp J, Wittig B, Bohr H, Kneipp K. Surface-enhanced Raman scattering: a new optical probe in molecular biophysics and biomedicine. *Theor Chem Acc* 2010;125:319-27.
100. Zavaleta CL, Smith BR, Walton I, Doering W, Davis G, Shojai B, et al. Multiplexed imaging of surface enhanced Raman scattering nanotags in living mice using noninvasive Raman spectroscopy. *Proc Natl Acad Sci U S A* 2009;106:13511-6.
101. Kennedy DC, Hoop KA, Tay LL, Pezacki JP. Development of nanoparticle probes for multiplex SERS imaging of cell surface proteins. *Nanoscale* 2010;2:1413-6.
102. Maiti KK, Samanta A, Vendrell M, Soh KS, Olivo M, Chang YT. Multiplex cancer cell detection by SERS nanotags with cyanine and triphenylmethine Raman reporters. *Chem Commun (Camb)* 2011;47:3514-6.
103. Alessandri I, Ferroni M, Depero LE. In situ plasmon-heating-induced generation of Au/TiO₂ "hot spots" on colloidal crystals. *Chemphyschem* 2009;10:1017-22.
104. Li W, Camargo PH, Lu X, Xia Y. Dimers of silver nanospheres: facile synthesis and their use as hot spots for surface-enhanced Raman scattering. *Nano Lett* 2009;9:485-90.
105. Li JF, Huang YF, Ding Y, Yang ZL, Li SB, Zhou XS, et al. Shell-isolated nanoparticle-enhanced Raman spectroscopy. *Nature* 2010;464:392-5.
106. Küstner B, Gellner M, Schutz M, Schoppler F, Marx A, Strobel P, et al. SERS labels for red laser excitation: silica-encapsulated SAMs on tunable gold/silver nanoshells. *Angew Chem Int Ed Engl* 2009;48:1950-3.
107. Brown LO, Doorn SK. A controlled and reproducible pathway to dye-tagged, encapsulated silver nanoparticles as substrates for SERS multiplexing. *Langmuir* 2008;24:2277-80.

108. Bao F, Yao JL, Gu RA. Synthesis of magnetic Fe₂O₃/Au core/shell nanoparticles for bioseparation and immunoassay based on surface-enhanced Raman spectroscopy. *Langmuir* 2009;25:10782–7.
109. Roca M, Haes AJ. Silica-void-gold nanoparticles: temporally stable surface-enhanced Raman scattering substrates. *J Am Chem Soc* 2008;130:14273–9.
110. Lim DK, Jeon KS, Hwang JH, Kim H, Kwon S, Suh YD, et al. Highly uniform and reproducible surface-enhanced Raman scattering from DNA-tailorable nanoparticles with 1-nm interior gap. *Nat Nanotechnol* 2011;6:452–60.
111. Vidyasagar MS, Maheedhar K, Vadhira BM, Fernandes DJ, Kartha VB, Krishna CM. Prediction of radiotherapy response in cervix cancer by Raman spectroscopy: a pilot study. *Biopolymers* 2008;89:530–7.
112. Chan JW, Taylor DS, Zwerdling T, Lane SM, Ihara K, Huser T. Micro-Raman spectroscopy detects individual neoplastic and normal hematopoietic cells. *Biophys J* 2006;90:648–56.
113. Short KW, Carpenter S, Freyer JP, Mourant JR. Raman spectroscopy detects biochemical changes due to proliferation in mammalian cell cultures. *Biophys J* 2005;88:4274–88.
114. Teh SK, Zheng W, Ho KY, Teh M, Yeoh KG, Huang Z. Diagnostic potential of near-infrared Raman spectroscopy in the stomach: differentiating dysplasia from normal tissue. *Br J Cancer* 2008;98:457–65.
115. Lau DP, Huang Z, Lui H, Anderson DW, Berean K, Morrison MD, et al. Raman spectroscopy for optical diagnosis in the larynx: preliminary findings. *Lasers Surg Med* 2005;37:192–200.
116. Crow P, Molckovsky A, Stone N, Uff J, Wilson B, WongKeeSong LM. Assessment of fiberoptic near-infrared Raman spectroscopy for diagnosis of bladder and prostate cancer. *Urology* 2005;65:1126–30.
117. Adams MJ, Royal Society of Chemistry (Great Britain). *Chemometrics in analytical spectroscopy*. 2nd ed. Cambridge: Royal Society of Chemistry; 2004.
118. Jess PR, Smith DD, Mazilu M, Dholakia K, Riches AC, Herrington CS. Early detection of cervical neoplasia by Raman spectroscopy. *Int J Cancer* 2007;121:2723–8.
119. Schlücker S, Kustner B, Punge A, Bonfig R, Marx A, Strobel P. Immuno-Raman microspectroscopy: in situ detection of antigens in tissue specimens by surface-enhanced Raman scattering. *J Raman Spectrosc* 2006;37:719–21.
120. Das K, Stone N, Kendall C, Fowler C, Christie-Brown J. Raman spectroscopy of parathyroid tissue pathology. *Lasers Med Sci* 2006;21:192–7.
121. Teh SK, Zheng W, Ho KY, Teh M, Yeoh KG, Huang Z. Diagnosis of gastric cancer using near-infrared Raman spectroscopy and classification and regression tree techniques. *J Biomed Opt* 2008;034013:13.
122. Lewis IR, Edwards HGM. *Handbook of Raman spectroscopy: from the research laboratory to the process line*. New York: Marcel Dekker; 2001.
123. Hanlon EB, Manoharan R, Koo TW, Shafer KE, Motz JT, Fitzmaurice M, et al. Prospects for in vivo Raman spectroscopy. *Phys Med Biol* 2000;45:R1–59.